Modelling of van der Waals force with smoothed particle hydrodynamics: application to the rupture of thin liquid films

Xiaoyang Xu [a, d, b, *], Mohar Dey [b], Mingfeng Qiu [b], James J. Feng [b, c, *]

[a] School of Computer Science and Technology, Xi'an University of Science and Technology, Xi'an 710054, China

[b] Department of Mathematics, University of British Columbia, Vancouver, BC, Canada

[c] Department of Chemical and Biological Engineering, University of British Columbia, Vancouver, BC, Canada

[d] School of Mathematics and Computer Science, Shaanxi University of Technology, Hanzhong, China

_____

Abstract

The rupture of thin liquid films driven by the van der Waals force is of significance in many engineering processes, and most previous studies have relied on the lubrication approximation. In this paper, we develop a smoothed particle hydrodynamics (SPH) representation for the van der Waals force and simulate the rupture of thin liquid films without resort to lubrication theory. The van der Waals force in SPH is only imposed on one layer, *i.e.*, the outermost layer of fluid particles, where a weighting function is deployed to evaluate the contributions of particles on or near the interface. However, to obtain an accurate hydrostatic pressure in reaction to the van der Waals force, a smaller smoothing length is used for the calculation of the weighting function than that used for SPH discretizations of the bulk fluid. The same surface particles are also used to model the surface tension. To deal with the rupture of a thin liquid film with a very small aspect ratio ε (ε = thickness/length), a coordinate transformation is introduced to shrink the length of the liquid film to achieve accurate numerical resolution with a manageable number of particles. As verifications of our physical model and numerical algorithm, we simulate the hydrostatic pressure in a stationary film and the relaxation of an initially square droplet and compare the SPH results with the analytical solutions. The method is then applied to simulate the rupture of thin liquid films with moderate and small aspect ratios (ε = 0.5 and 0.005). The convergence of the method is verified by refining particle spacing to four different levels. The effect of the capillary number on the rupture process is analyzed.

Keywords

SPH; van der Waals force; surface tension; thin liquid film; coordinate transformation

_____

1. Introduction

The van der Waals force [1] can cause a thin liquid film to rupture and form a dry spot on a solid substrate despite the stabilizing effect of surface tension. Such phenomena are common in daily life and engineering applications such as coating flow [2], hard disk driver [3], foam stability [4], and rupture of the tear film in the eye [5, 6]. Understanding the rupturing mechanism of thin liquid films is of great significance. Up to now, the rupture of thin liquid films has been mostly studied using lubrication theory, where the long-wave equations of motion for the free surface rupture are derived from the Navier–Stokes equations. For example, Ruckenstein and Jain [7] studied the spontaneous rupture of a thin liquid film on a

---

*Corresponding authors.

E-mail addresses: xiaoyang.xu@xust.edu.cn (Xiaoyang Xu), james.feng@ubc.ca (J.J. Feng).

solid substrate by hydrodynamic stability theory. The motion of the liquid film was generated by a small perturbation of the free interface, and the van der Waals force was calculated from the potential energy per unit volume in the liquid caused by the London–van der Waals interactions with the surrounding molecules of the liquid and with those of the solid. Williams and Davis [8] examined nonlinear effects on film rupture by investigating the stability of thin films to finite amplitude disturbances. They derived a nonlinear partial differential equation for the film thickness and solved it by numerical methods as an initial-value problem with periodic boundary conditions in the longitudinal direction. Zhang and Lister [9] showed that the rupture of a thin viscous film on a solid substrate possessed a countably infinite number of similarity solutions. Conroy et al. [10] explored the influence of electrokinetics on the dynamics of an annular electrolyte film that surrounds a perfectly conducting fluid core in a horizontal cylinder. Garg et al. [11] analyzed thinning and rupture of a thin film of a power-law fluid on a solid substrate under a destabilizing van der Waals pressure and a stabilizing capillary pressure.

The case analyzed by the lubrication theory is simplified as it is limited to small surface deformation and in principle fails toward the final stage of rupture. Besides, there are films with complex structures such as solute redistribution or phase separation [5, 6], which require a resolution of the thickness direction. Beyond the lubrication approximation, there are mainly two kinds of numerical methods for solving the full Navier–Stokes equations. One is grid-based, examples being the finite difference, finite volume, and finite element methods. These methods are mature, but the underlying grids may encounter difficulties in representing the moving interfaces in complex problems. To track the interfaces, some techniques (*e.g.* volume of fluid [12], marker and cell [13] and level set [14]) are usually implemented together with the Navier-Stokes solver. Moreover, interfacial rupture requires ad hoc treatment in grid-based methods [15]. The other is the meshfree particle methods [15], which have been developed and applied to a range of flow simulations in recent decades. A remarkable feature of this class of methods is that the governing equations are solved on a set of discretized particles with no underlying meshes. Indeed, meshless particle methods have some advantages over grid-based methods: it handles the convection dominated flows without numerical diffusion; it is well-suited for the simulations of large-deformation flows and programming can be easier than in grid-based methods. As a typical meshfree particle method, smoothed particle hydrodynamics (SPH) [16, 17] is originally proposed to model the astrophysical problems. Recently, it has been applied in a wide range of research areas such as the mechanics of red blood cell [18], coastal hydrodynamics [19], explosion [20, 21], fluid-solid interactions [22], multiphase flows [23], and viscoelastic flows [24−27], among others.

When simulating the rupture of thin liquid films, the surface tension plays an important role. In general, there are two ways to model the surface tension in SPH. One is based on the cohesive pressure of the van der Waals equation of state. Nugent and Posch [28] applied it to drop condensation of a two-dimensional van der Waals fluid. Tartakovsky and Meakin [29] used a cosine model by applying the interaction of fluid–fluid and fluid–solid particles for simulating surface tension and contact angle. The other is the continuum surface force (CSF) method proposed by Brackbill et al. [30]. Morris [31] developed the CSF model in SPH to simulate two-phase flows and tested the numerical method on simple benchmark

problems with equal density and viscosity. Hu and Adams [32] applied it to incompressible multiphase flow. The method produced excellent results in the simulation of droplet oscillation, contact angle, droplet deformation in shear flow, and Rayleigh–Taylor instability. Grenier et al. [33] derived another multiphase SPH model for simulations of free surface problems from a Lagrangian variational approach. More recent developments have extended SPH treatments of surface tension to high density and viscosity ratios [34–36], indicating that SPH can simulate interfacial dynamics accurately. However, to the authors' best knowledge, no meshfree particle methods have been developed for modelling the van der Waals force or simulating the rupture of a thin liquid film.

This paper presents an SPH model for the rupture of a thin liquid film on a solid substrate driven by the van der Waals force. Unlike some previous lubrication-based solutions, the rupture of thin liquid films is computed directly from the Navier–Stokes equations, which can be recognized as an important step of SPH towards a new class of physical problems. The van der Waals force is only imposed on the outmost layer of fluid particles, where a weighting function is deployed to evaluate the contributions of particles on or near the interface. However, one notable point is that the weighting function is computed with a smaller smoothing length than that used in the bulk, which is found to be important for accurately reproducing the hydrostatic pressure. The same surface particles are also used to model the surface tension, which stabilizes the rupture of the liquid film. To deal with the rupture of a thin liquid film with a very small aspect ratio, we introduce a coordinate transformation along the longitudinal x-axis, $x = \tan(\xi)$. This technique is used to avoid deploying a large number of fluid particles far from the region of the rupture, and thus the computational cost is dramatically reduced.

The rest of this paper is structured as follows: Section 2 describes the mathematical formulations as well as the numerical method implemented. In Section 3, selected numerical examples are simulated and compared against available results in the literature. We conclude the paper with a final remark in Section 4.

2. Mathematical formulations

2.1 Governing equations

In a Lagrangian frame, the governing equations for weakly compressible viscous flow are:

$$\frac{d\rho}{dt} = -\rho \nabla \cdot \mathbf{u} , \tag{1}$$

$$\rho \frac{d\mathbf{u}}{dt} = \nabla \cdot \mathbf{\sigma} + \mathbf{F}_s + \mathbf{F}_v , \tag{2}$$

$$\frac{d\mathbf{r}}{dt} = \mathbf{u} , \tag{3}$$

where ρ is the density, t the time, $\mathbf{u}$ the velocity, $\mathbf{\sigma}$ the total stress tensor, and $\mathbf{r}$ the position. $\mathbf{F}_s$ and $\mathbf{F}_v$ are surface tension and van der Waals force per unit volume, respectively, whose formulation will be explained in Sections 2.3 and 2.4. The symbol d/dt is the material derivative operator, $d/dt = \partial/\partial t + \mathbf{u} \cdot \nabla$.

3

The total stress tensor $\boldsymbol{\sigma}$ is usually decomposed into an isotropic pressure and a viscous stress:

$$\boldsymbol{\sigma} = -p\mathbf{I} + 2\eta\mathbf{D}, \tag{4}$$

where $\mathbf{I}$ is the unit tensor, η the dynamic viscosity, and $\mathbf{D}$ the rate-of-deformation tensor

$$\mathbf{D} = \frac{1}{2}\left(\nabla\mathbf{u} + (\nabla\mathbf{u})^{\mathrm{T}}\right). \tag{5}$$

The governing equations are not closed at this stage. It is common to use a suitable equation of state to describe the variation of pressure with density. We use the following equation of state [37]:

$$p(\rho) = \frac{\rho_0 c_0^2}{\gamma}\left(\left(\frac{\rho}{\rho_0}\right)^{\gamma} - 1\right), \tag{6}$$

where c_0 is the speed of sound, $\gamma = 7$ is a constant, and ρ_0 is the initial density of the fluid. To ensure the flow behavior of the pseudo-compressible fluid is sufficiently close to that of a truly incompressible fluid, the sound speed c_0 is usually chosen to be at least 10 times higher than the maximal fluid velocity [38].

2.2 SPH formulations

The SPH method approximates an arbitrary function $A(\mathbf{r})$ by the following integral:

$$\langle A(\mathbf{r})\rangle = \int_{\Omega} A(\mathbf{r}')W(\mathbf{r} - \mathbf{r}', h)d\mathbf{r}', \tag{7}$$

where W is an interpolation kernel function, and h is the smoothing length defining the supporting domain of the kernel. In this paper, the quintic Wendland kernel [39] is chosen as its continuous second derivative affords better accuracy and stability:

$$W(r, h) = \alpha_D \times \begin{cases} (2-q)^4(1+2q) & 0 \leq q < 2 \\ 0 & q \geq 2 \end{cases}, \tag{8}$$

where the normalization factor α_D takes the value of $7/64\pi h^2$ in 2D space, $q = r/h$, and $r = |\mathbf{r} - \mathbf{r}'|$ is the distance between two particles.

In SPH, the fluid is discretized by a set of particles which follow the fluid motion. Each particle has its own mass, density, pressure, and velocity. The motion of a particle of interest is affected by its neighboring particles within the supporting domain. The particle approximation for the function $A(\mathbf{r})$ at particle a can be obtained as follows:

$$A(\mathbf{r}_a) = \sum_b V_b A(\mathbf{r}_b)W_{ab}, \tag{9}$$

where $W_{ab} = W(|\mathbf{r}_a - \mathbf{r}_b|, h)$, $V_b = m/\rho_b$ is the volume of particle b, and m is the particle mass. The particle approximation for the spatial derivative $\nabla \cdot A(\mathbf{r})$ is similarly obtained as:

$$\nabla \cdot A(\mathbf{r}_a) = \sum_b V_b A(\mathbf{r}_b) \cdot \nabla_a W_{ab}, \tag{10}$$

where ∇_a is the gradient operator with respect to the particle a.

Note that we can use several different ways to further derive the spatial derivative, $e.g.$,

4

$$\nabla \cdot A(\boldsymbol{r}) = \frac{1}{\rho}\left(\nabla \cdot (\rho A(\boldsymbol{r})) - A(\boldsymbol{r}) \cdot \nabla \rho\right), \tag{11}$$

$$\nabla \cdot A(\boldsymbol{r}) = \rho\left(\nabla \cdot \left(\frac{A(\boldsymbol{r})}{\rho}\right) + \frac{A(\boldsymbol{r})}{\rho^2} \cdot \nabla \rho\right). \tag{12}$$

By applying Eq. (10) to Eqs. (11) and (12), we obtain the following particle approximations for the spatial derivative:

$$\nabla \cdot A(\boldsymbol{r}_a) = \frac{1}{\rho_a}\sum_b m\left(A(\boldsymbol{r}_b) - A(\boldsymbol{r}_a)\right) \cdot \nabla_a W_{ab}, \tag{13}$$

$$\nabla \cdot A(\boldsymbol{r}_a) = \rho_a\left(\sum_b m\left(\frac{A(\boldsymbol{r}_b)}{\rho_b^2} + \frac{A(\boldsymbol{r}_a)}{\rho_a^2}\right) \cdot \nabla_a W_{ab}\right), \tag{14}$$

respectively. In these two particle approximations, $A(\mathbf{r})$ appears pairwise and exhibits anti-symmetry and symmetry, respectively, between particles a and b. These features help to improve the numerical accuracy and stability in SPH simulations [38].

In this paper, the continuity and momentum equations are respectively discretized based on Eqs. (13) and (14), so we have [45]:

$$\frac{d\rho_a}{dt} = \sum_b m(\mathbf{u}_a - \mathbf{u}_b) \cdot \nabla_a W_{ab}, \tag{15}$$

$$\left(\frac{d\mathbf{u}}{dt}\right)_a = \sum_b m\left(\frac{\boldsymbol{\sigma}_a}{\rho_a^2} + \frac{\boldsymbol{\sigma}_b}{\rho_b^2}\right) \cdot \nabla_a W_{ab} + \frac{1}{\rho_a}\mathbf{F}_s + \frac{1}{\rho_a}\mathbf{F}_v. \tag{16}$$

When computing the discretized Eqs. (15) and (16), the smoothing length h should be taken to be slightly larger than the initial particle spacing Δx [15]. In this paper, $h = 1.5\Delta x$ is used unless otherwise specified.

Furthermore, in order to improve the computational accuracy and suppress spurious oscillations in the pressure field, we implement a corrected kernel gradient [40–43] and also introduced a Rusanov flux into the continuity equation [44]. Now the discretized Eqs. (15) and (16) are rewritten as [45]:

$$\frac{d\rho_a}{dt} = \sum_b m\left((\mathbf{u}_a - \mathbf{u}_b) + \hat{\mathbf{r}}_{ab}\left(\frac{c_{ab}}{\rho_b}(\rho_b - \rho_a)\right)\right) \cdot \nabla_a \tilde{W}_{ab}, \tag{17}$$

$$\left(\frac{d\mathbf{u}}{dt}\right)_a = \sum_b m\left(\frac{\boldsymbol{\sigma}_a}{\rho_a^2} + \frac{\boldsymbol{\sigma}_b}{\rho_b^2}\right) \cdot \nabla_a \tilde{W}_{ab} + \frac{1}{\rho_a}\mathbf{F}_s + \frac{1}{\rho_a}\mathbf{F}_v, \tag{18}$$

where $\nabla_a \tilde{W}_{ab}$ denotes the corrected kernel gradient defined by:

$$\nabla_a \tilde{W}_{ab} = \mathbf{M}_a^{-1}\nabla_a W_{ab}, \tag{19}$$

and $\mathbf{M}_a$ is the correction matrix

$$\mathbf{M}_a = \sum_b V_b \nabla_a W_{ab} \otimes (\mathbf{r}_b - \mathbf{r}_a). \tag{20}$$

Moreover, in the second right-hand-side term of Eq. (17), $\hat{\mathbf{r}}_{ab}$ is the unitary vector of the distance between particles a and b defined by:

$$\hat{\mathbf{r}}_{ab} = \frac{\mathbf{r}_b - \mathbf{r}_a}{r_{ab}}, \tag{21}$$

c_{ab} is the maximum numerical speed of sound between particle a and b, $i.e.$,

$$c_{ab} = \max\left(c_a, c_b\right), \tag{22}$$

with

$$c_a = \sqrt{\frac{\partial P_a}{\partial \rho_a}} = c_0 \left(\frac{\rho_a}{\rho_0}\right)^{\frac{\gamma-1}{2}}. \tag{23}$$

For more details on the discretization of the governing equations, we refer the reader to the previous works of Xu and Deng [45].

To solve the system of governing equations along the particle paths, a two-step predictor-corrector scheme [15] is adopted. Let $\mathbf{q}_a$ denotes the unknown variables $\left(\rho_a, \mathbf{u}_a, \mathbf{r}_a\right)$, and $\mathbf{F}(\mathbf{q}_a)$ the force vector on the right-hand side. The predictor step at each time interval is an explicit Eulerian evaluation of $\mathbf{q}_a$, $i.e.$, $\mathbf{q}_a^{n+1/2} = \mathbf{q}_a^n + \mathbf{F}\left(\mathbf{q}_a^n\right)\Delta t / 2$. In the corrector step, the final corrected value of $\mathbf{q}_a$ is calculated by $\mathbf{q}_a^{n+1} = \mathbf{q}_a^n + \mathbf{F}\left(\mathbf{q}_a^{n+1/2}\right)\Delta t$. Moreover, in order to maintain numerical stability, several time step constraints must be satisfied, including a Courant–Friedrichs–Lewy condition [15]:

$$\Delta t \le 0.5 \frac{h}{c_0}, \tag{24}$$

a viscous diffusion condition [38]:

$$\Delta t \le 0.125 \frac{h^2}{\upsilon_0}, \tag{25}$$

and a surface tension condition [30, 32]:

$$\Delta t \le 0.25 \left(\frac{\rho h^3}{2\pi\beta}\right)^{1/2}, \tag{26}$$

where $\upsilon_0 = \eta / \rho_0$ is the kinematic viscosity and β the surface tension coefficient.

2.3 Van der Waals force modelling in SPH

The van der Waals force stems from the attraction between molecules and atoms in close proximity, and it is important for the rupture of thin liquid films [1]. Several research groups have studied the rupture of thin liquid films driven by the van der Waals force, almost always using the lubrication approximation [5–11]. In this work, we will not resort to the lubrication approximation but will model the van der Waals force directly within the Navier-Stokes equations in 2D. To the authors' knowledge, this is the first time that the van der Waals force is modelled within the framework of SPH.

For a liquid film of thickness H between parallel surfaces, the intermolecular attractive van der Waals force between the two surfaces can be represented by a normal stress on the surface or a disjoining pressure

inside the film [1, 6]:

$$\Pi = \frac{A}{6\pi H^3},$$
(27)

where A is the unretarded Hamaker constant. In the lubrication formalism, such a term is incorporated into the momentum equation as a potential akin to gravity. However, in SPH, a more natural representation would be to impose a surface force $\mathbf{f}_v$ onto the outmost layer of fluid particles, pointing vertically toward the substrate with a magnitude of Π, see Fig. 1. The surface force $\mathbf{f}_v$ per unit area is thus given by

$$\mathbf{f}_v = \left(0, -\frac{A}{6\pi H^3}\right)^T,$$
(28)

where H can be taken as the difference of the y-coordinate of the outmost layer fluid particles to the solid substrate. We impose such a surface force even when the free surface of the liquid film deviates from the horizontal. A complication arises in implementation, however. A dynamically deforming surface can become rough so it becomes ambiguous which particles constitute the "outermost layer". To resolve this problem, we introduce a weighting function λ to spread the surface force $\mathbf{f}_v$ into a volume force $\mathbf{F}_v$ concentrated on the interface:

$$\mathbf{F}_v = \mathbf{f}_v \cdot \lambda.$$
(29)

The weighting function λ is defined on each particle and is nonzero only for those at the interface. In principle, λ should be designed such that it reproduces the correct total amount of surface force on rough surfaces by properly weighing the contributions of particles at the nominal surface, as illustrated in Fig. 2. Therefore, no matter a smooth surface or a rough surface, λ should recover $\mathbf{f}_v$ only on the surface layer of particles, without spreading onto any interior particles. Indeed, the weighting function λ peaks at the interface and is an approximation to the Dirac delta-function concentrated at the fluid interface.
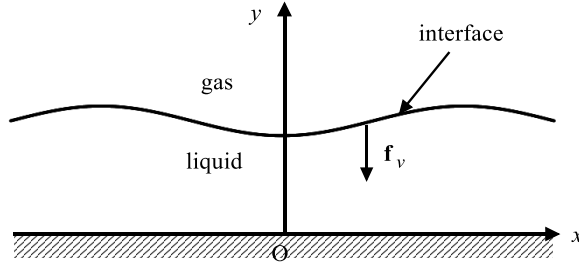

Fig. 1 Sketch of the van der Waals force $\mathbf{f}_v$: the force direction is perpendicular to the substrate.

The design of λ follows two steps. In the first step, we use the decreased particle density on or near the surface as a coarse criterion to identify potential "surface particles":

$$\rho_a^* < 0.97 \cdot \rho_0,$$
(30)

where the particle density is calculated by the summation method:

$$\rho_a^* = \sum_b m \cdot W_{ab}.$$
(31)

This detection is inexact in that some inner particles may be counted as surface particles [46]. In the second

7

step, we apply a finer criterion based on the magnitude of the gradient of the particle concentration. For a target particle a that has been marked at the first step, the gradient of the particle concentration is computed by:

$$\nabla\Gamma_a = \sum_b V_b \nabla_a \tilde{W}_{ab}.$$

(32)

It should be noted that the gradient of the particle concentration will have a larger magnitude for particles on or near the interface, and will nearly vanish for interior points. Once $\nabla\Gamma_a$ is computed, the actual free surface particles used to model van der Waals force can be filtered by

$$\left|\nabla\Gamma_a\right| > \Lambda \cdot \frac{1}{\Delta x},$$

(33)

where Λ is a constant used to control the inclusion of particles near the free surface for computing the van der Waals force. Effectively it defines which particles constitute the outmost layer. Our numerical experiments show that the range of $0.15 < \Lambda < 0.25$ would be a good choice. In this work, we have used $\Lambda = 0.2$, and particles satisfying this condition are regarded as the outmost layer of particles forming the free surface.
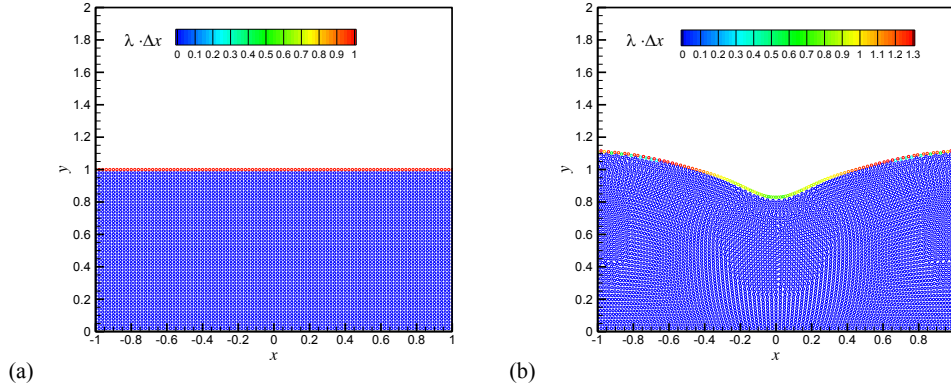

Fig. 2 The weighting function λ for (a) a smooth surface and (b) a dynamically deforming surface.

Finally, for the surface particles thus determined, we define the weighting function λ simply as:

$$\lambda_a = \left|\nabla\Gamma_a\right|.$$

(34)

However, special attention should be paid to the choice of the smoothing length used for the calculation of the weighting function. Specifically, when computing Eqs. (29)–(34), a smaller smoothing length of $h_2 = 1.0\Delta x$ should be used in order to reproduce accurately the hydrostatic pressure in the interior. This is in contrast with $h = 1.5\Delta x$ used for SPH discretizations of the bulk fluid. Indeed, to reproduce the correct amount of van der Waals force, the weighting function λ calculated should be strictly equal to $1/\Delta x$ since only one layer of fluid particles is used. As illustrated in Section 3.1, our numerical experimentations have shown that the Λ and h_2 values adopted here reproduce the correct amount of van der Waals force in our SPH model that corresponds to the classic formula for the disjoining pressure in Eq. (27).

2.4 Surface tension

Our surface tension model is similar to that of Morris [31] in that it attempts to estimate the curvature of the interface between fluids of different phases. However, unlike Morris [31], we do not utilize several layers of fluid particles, but take advantage of the same particles already used for the van der Waals force to model the surface tension. Therefore, $\mathbf{F_s}$ applies only to the outmost layer of fluid particles and is computed by $\mathbf{F}_s = \mathbf{f}_s \cdot \lambda$ with a surface force $\mathbf{f}_s$ and the same weight function λ. Following [31], we model the surface force $\mathbf{f}_s$ as:

$$\mathbf{f}_s = \beta \kappa \hat{\mathbf{n}}, \tag{35}$$

where β is the surface tension coefficient, κ the interface curvature, and $\hat{\mathbf{n}}$ the unit normal vector to the interface. We further assume that there is no surface gradient of interfacial tension, and neglect Marangoni stresses.

To calculate the unit normal vector to the interface, we define a color function c that is unity in the interior of the fluid but declines near the interface for the deficiency of neighbors in the gaseous phase:

$$c_a = \sum_b V_b W_{ab}. \tag{36}$$

The surface normal can be estimated as a gradient of the color function

$$\mathbf{n} = \nabla c, \tag{37}$$

and

$$\hat{\mathbf{n}} = \frac{\mathbf{n}}{|\mathbf{n}|}. \tag{38}$$

The interface curvature is defined as

$$\kappa = -\nabla \cdot \hat{\mathbf{n}}. \tag{39}$$

In SPH, the discrete approximations of Eqs. (37) and (39) can be written as [31]

$$\mathbf{n}_a = \sum_b V_b (c_b - c_a) \nabla_a \tilde{W}_{ab}, \tag{40}$$

and

$$\kappa = -\sum_b V_b \left(\hat{\mathbf{n}}_b - \hat{\mathbf{n}}_a\right) \cdot \nabla_a \tilde{W}_{ab}. \tag{41}$$

It is well-known that the deficiency of particles on or near the free surface would significantly affect the SPH computation, *e.g.*, the evaluation of the interface curvature. Morris [31] resolved this problem with an additional normalization of the curvature (see Eq. (23) in [31]), while Adami et al. [47] used a new reproducing divergence approximation to solve the curvature. Since we have employed the kernel gradient correction that reduces the effects of the deficiency of particles on or near the free surface, the techniques presented in [31, 47] are not needed here. Moreover, as mentioned before, only the outmost layer of fluid particles are employed to model the surface tension. Therefore, unlike Morris [31], there is also no need to use the special criteria (see Eq. (20) in [31]) to filter the normal vectors that lead to spurious directions and magnitudes of the surface tension.

2.5 The coordinate transformation

Thin liquid films typically have very small height-to-length aspect ratios, and the rupture proceeds through highly localized deformation of the interface. To adequately resolve the rupture in SPH, one would need to deploy the same fine spatial resolution for the entire length, incurring prohibitive computational costs. To address this difficulty, we transform the x-coordinate along the length of the film: $x = \tan(\xi)$, so as to shrink the length for regions far from the origin, where the rupture happens. Fig. 3 shows a schematic for a thin film of aspect ratio $\varepsilon = 0.005$. With this transformation, a uniform initial spacing of SPH particles in the (ξ, y) domain corresponds to the same resolution near the region of rupture ($x = 0$) in the (x, y) domain, and increasingly coarse resolution toward the left and right ends. Therefore, we avoid deploying dense particles in regions of little dynamics and can achieve accurate numerical resolution with a manageable number of particles.
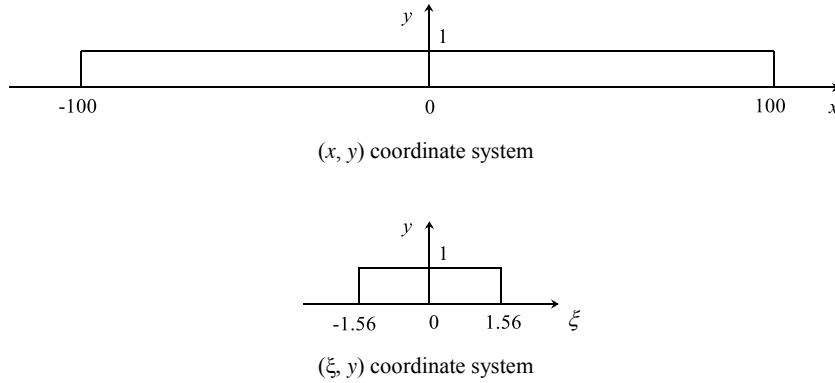

(x, y) coordinate system

(ξ, y) coordinate system

Fig. 3 Schematic diagram for the coordinate transformation along the longitudinal x-axis, $x = \tan(\xi)$.

With $x = \tan(\xi)$, the governing equations for the rupture of thin liquid film are transformed accordingly. In terms of the new coordinates (ξ, y), the governing equations are written as

$$\frac{d\rho}{dt} = -\rho\left(\cos^2 \xi \cdot \frac{\partial u}{\partial \xi} + \frac{\partial v}{\partial y}\right), \tag{42}$$

$$\rho\frac{du}{dt} = \cos^2 \xi \cdot \frac{\partial \sigma^{\xi\xi}}{\partial \xi} + \frac{\partial \sigma^{\xi y}}{\partial y} + F_s^\xi + F_v^\xi, \tag{43}$$

$$\rho\frac{dv}{dt} = \cos^2 \xi \cdot \frac{\partial \sigma^{\xi y}}{\partial \xi} + \frac{\partial \sigma^{yy}}{\partial y} + F_s^y + F_v^y, \tag{44}$$

$$\frac{d\xi}{dt} = \cos^2 \xi \cdot u, \tag{45}$$

$$\frac{dy}{dt} = v, \tag{46}$$

where

$$\sigma^{\xi\xi} = -p + \cos^2 \xi \cdot 2\eta \frac{\partial u}{\partial \xi}, \tag{47}$$

$$\sigma^{\xi y} = \sigma^{y\xi} = \eta \left(\frac{\partial u}{\partial y} + \cos^2 \xi \cdot \frac{\partial v}{\partial \xi} \right), \tag{48}$$

$$\sigma^{yy} = -p + 2\eta \frac{\partial v}{\partial y}. \tag{49}$$

Now the new system of governing equations can be solved by the SPH method presented in Section 2.2. We also don't need to modify the computational of the kernel, since the largest surface deformation of the film occurs around $x = 0$. Indeed, at this region, the particle distribution in the (ξ, y) domain corresponds to almost the same particle distribution in the (x, y) domain. There are negligible errors around $x = 0$ between the (ξ, y) and (x, y) solutions. Therefore, the rupture of the liquid film can be perfectly captured. For the left and right ends of liquid film, there are no large surface deformations because of the very great length of the film in the physical (x, y) domain. Therefore, we can still capture the flow physics of both ends of liquid film, although the error of the kernel at both ends of liquid film is comparatively large. Moreover, we highlight that such transformation has been used successfully in grid-based numerical methods [6, 48, 49], but we have not found any SPH implementations in the literature. The numerical accuracy of SPH using the coordinate transformation will be tested in Section 3.3.

2.6 Boundary condition

In this paper, two types of boundary conditions, *i.e.*, periodic boundary and wall boundary conditions are involved. For the former, it can be simply implemented as particles going out of the liquid domain from one end will enter into the other end. While for the wall boundary condition, we follow our previous work [51, 52] and adopt two types of virtual particles, *i.e.*, wall particles and dummy particles. Specifically, only one layer of wall particles are regularly placed on the solid wall with an initial particle spacing Δx. Wall particles do not exert a repulsive force to prevent fluid particles from penetrating the solid substrate. Instead, they contribute to SPH calculations for the velocity, density, and pressure. The density and positions of wall particles are always unchanged during the simulations. The pressure of a wall particle a is calculated by

$$p_a = \frac{\sum_b V_b p_b W_{ab}}{\sum_b V_b W_{ab}}, \tag{50}$$

where a denotes a wall particle and b represents its neighboring fluid particles only.

Dummy particles are placed outside the solid wall by duplicating wall particles out of the fluid domain in the normal direction, at a distance Δx from the solid wall. In principle, the dummy particles should fill a domain with at least a range of depth comparable with the supporting domain of the kernel. Accordingly, three-layer dummy particles are included in this paper. Similar to wall particles, dummy particles also have fixed density and positions. Besides, each dummy particle is associated with a wall particle in the normal direction of the solid wall. As such, a mirrored point along the associated wall particle for dummy particle can be easily placed inside the fluid domain. Thereupon, the velocity of the mirrored point could be

similarly calculated according to Eq. (50). To implement the no-slip boundary condition along the solid wall, the velocity of each wall particle is set to be zero and the velocity of each dummy particle is reversed with its corresponding mirrored point. While for the pressure field along the solid wall, the homogeneous Neumann condition is applied, *i.e.*, the pressure of a dummy particle is set to that of a wall particle associated with it.

3. Results

In this section, we first use a hydrostatic calculation to validate the proposed SPH method in modelling the van der Waals force. Then, we simulate the shape relaxation of a drop from a square initial shape, which establishes the accuracy of the proposed SPH model for surface tension. Lastly, the proposed SPH method is applied to study the rupture of thin liquid films on a solid substrate. In all numerical examples, we have employed dimensionless parameters to facilitate the flow analysis.

3.1 Hydrostatic test

The hydrostatic test is a benchmark problem and has been numerically studied using SPH by Adami et al. [50]. In this paper, we consider a variant of the hydrostatic test [50], in which the hydrostatic pressure is not due to a body force like gravity but due to a van der Waals force. Since the van der Waals force is only imposed on the outmost layer of fluid particles, a uniform and constant pressure field should develop in the bulk of the liquid as a result.

The computational domain is chosen as: $-1 < x < 1$, $0 < y < 1$, so we have the width and height of liquid as $L = 2$ and $H = 1$, respectively. The fluid density is $\rho_0 = 1$, and its dynamic viscosity is $\eta = 1$. The space above the liquid is empty and we do not deploy SPH particles there to represent, for example, air. The total number of fluid particles used is 5000, with an initial particle spacing of $\Delta x = 0.02$. Similar to [50], we ignore surface tension in this benchmark problem. The force imposed on the surface of the liquid is downward toward the substrate: $\mathbf{f}_v = (0, 1)^\mathrm{T}$. This force is our analog of the van der Waals force, since it tests the same scheme for handling the van der Waals force in our SPH model. As stated in Section 2.3, we spread $\mathbf{f}_v$ into an equivalent volumetric force $\mathbf{F}_v$ using the weight function λ. The sound speed is chosen as $c_0 = 200$, while a time step of $\Delta t = 1 \times 10^{-5}$ is used to maintain numerical stability. The solid substrate is modelled using wall and dummy particles [51, 52], and no-slip boundary condition is imposed. Periodic boundary conditions are imposed on the left and right ends of the liquid domain [1, 6].

Initially, the particles are placed on a Cartesian lattice with the density equal to the reference density ρ_0, thus having zero pressure in the fluid phase. Then, driven by the van der Waals force, the surface particles move down slightly to compact the fluid, whose density increases. In response, the fluid pressure rises to balance the van der Waals force on the surface of liquid film. Therefore, after an initial transient phase, the particles settle down with a steady and constant pressure $p = 1$, see Fig. 4.
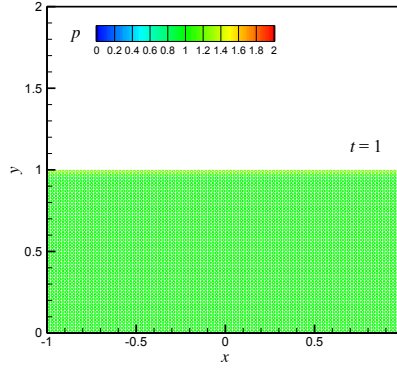
12

Fig. 4 The equilibrium solution of the hydrostatic test, achieved at $t = 1$. The interior develops a uniform pressure $p = 1$ in response to the van der Waals forces applied onto the surface particles.

Fig. 5a shows the development of the pressure at the origin $(0, 0)$ for three levels of spatial resolution $\Delta x = 0.04$, 0.02, and 0.01. Following Adami et al. [50], we have used the damping technique during the initial transient of simulations to reduce the spurious high-frequency oscillations due to pseudo-sound traveling through the domain. We define a damping time $t_{damp} = 0.5$ during which the van der Waals force is multiplied by the following factor:

$$\zeta(t) = 0.5\left[\sin\left(\left(-0.5 + t/t_{damp}\right)\pi\right) + 1\right], \quad t \leq t_{damp} . \tag{51}$$

This corresponds to a gradual buildup in the particle acceleration due to the van der Waals force. As seen, the pressure gradually reaches the expected level $p = 1$ in all simulations. The results are converged with respect to the spatial resolution. The steady state pressure is in excellent agreement with the expected value. The results of the benchmark have validated the proposed SPH model of the van der Waals force.

Moreover, as mentioned before, a smoothing length of $h = 1.5\Delta x$ is used for the SPH discretization of governing equations, while a smaller value of $h_2 = 1.0\Delta x$ is adopted when calculating the weight function λ. To illustrate the necessity of using such a small h_2, we have run three additional tests with $h_2 = 1.1\Delta x$, $1.3\Delta x$, and $1.5\Delta x$, with all other parameters fixed. Fig. 5b clearly shows that the larger h_2 incurs larger errors when compared to the expected pressure $p = 1$. When h_2 approaches the initial particle spacing Δx, the accurate hydrostatic pressure is recovered. Actually, to recover the true hydrostatic pressure, the weight function λ calculated should be strictly equal to $1/\Delta x$, because only one layer of fluid particles is used. With the wider $h_2 = 1.5\Delta x$, $1.3\Delta x$ and $1.1\Delta x$, the weighting function λ would be, respectively, 84.4%, 92.8%, and 99.5% of the expected amount $1/\Delta x$. These are consistent with the pressure level displayed in Fig. 5b. Therefore, we conclude that the choice of $h_2 = 1.0\Delta x$ for modelling the van der Waals force is reasonable, as it produces an accurate hydrostatic pressure in reaction to the van der Waals force. Of course, if the modified Gaussian kernel [53], where the kernel function is non-zero when $0 \leqslant q < 3$, is adopted, a more smaller $h_2 = 0.666\Delta x$ should be used in order to satisfy that the weight function λ calculated is strictly equal to $1/\Delta x$.
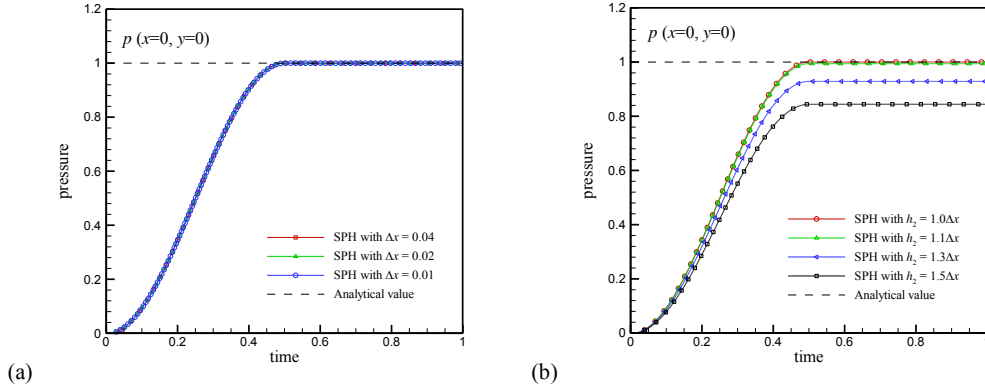
Fig. 5 The time history of pressure recorded at point (x=0, y=0): the influence of (a) initial particle spacing Δx and (b) smoothing length h_2 on the SPH solutions. The dash line indicates the expected value of p=1.

3.2 Relaxation of an initially square droplet

To validate the surface tension model, we simulate the relaxation of an initially square droplet. The main difference between our approach and previous studies [34, 47] is that we use only the outmost layer of fluid particles to model the surface tension. Moreover, unlike [34, 47], we do not consider the two-phase flow (*i.e.*, fluid and gas phase) with different density and viscosity ratios. Instead, only the fluid phase is represented and thus it corresponds to a situation of infinite density and viscosity ratio. However, we would like to highlight that even if no gas particles are included, satisfactory results can still be obtained by using our single-layer modelling of the surface tension.

As shown in Fig. 6a, the square droplet has a side length of $l_x = l_y = 1$ located at the center of a square computational domain. The fluid density is $\rho_0 = 1$, and the dynamics viscosity $\eta = 1$. The surface tension coefficient is set to be $\beta = 1$. We have tested two different levels of spatial resolution, with initial particle spacing $\Delta x = 0.025$ and 0.0125 and a total of 1600 and 6400 particles, respectively. The sound speed is chosen as $c_0 = 100$, while the time step of $\Delta t = 5 \times 10^{-5}$ is used to maintain numerical stability. Since no gas particles are used in the simulations, no wall boundary condition is needed on the outer walls of the domain.

Under the action of surface tension, the square droplet will gradually transform into a circular droplet to minimize its surface energy. Indeed, at $t = 1$, the steady-state drop shape is reached. It is nearly a perfect circle, as clearly seen in Fig. 6b. The steady-state Laplace pressure inside the droplet is expected to be:

$$\Delta P = \frac{\beta}{R} = \frac{\beta\sqrt{\pi}}{l_x}, \tag{52}$$

where R is the final radius of the droplet. Fig. 7 plots the time evolution of the average pressure of the droplet. It is observed that the pressure of the droplet gradually approaches a steady-state value as time goes on, which agrees with the analytical Laplace pressure to within 1.7% for the low resolution and within 0.3% for the fine one. The simulation results confirm the accuracy and convergence of our single-layer modelling of the surface tension. Moreover, when the steady state is reached, the velocity field in the entire

domain should be ideally zero. However, because of numerical errors, the velocity field never becomes precisely zero. Therefore, particles keep oscillating around their settled positions. This explains the slight pressure oscillation in Fig. 7.
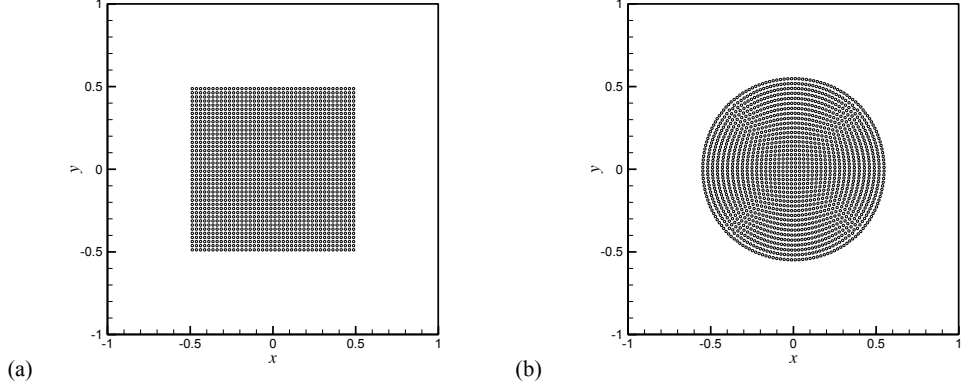

(a)   (b)

Fig. 6 Relaxation of an initially square droplet: (a) particle positions at $t = 0$, (b) particle positions at $t = 1$.
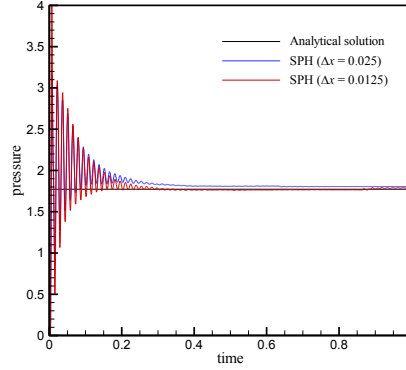

Fig. 7 The time evolution of the average pressure of the droplet.

3.3 The rupture of thin liquid films

In this section, we apply the proposed SPH model to simulate the rupture of thin liquid films on a solid substrate with an initial thickness H, length L, and aspect ratio $\varepsilon = H/L$. We choose the characteristic length as the initial thickness of the liquid film H, and define the characteristic velocity V and pressure P using the van der Waals force [1, 6, 54]:

$$V = \frac{A}{6\pi\eta H^2}, \quad P = \frac{A}{6\pi H^3},$$ (53)

as it is the driving force of the rupture. Accordingly, all other parameters and variables in the problem can be scaled as:

$$x = \frac{x^*}{H}, \quad y = \frac{y^*}{H}, \quad u = \frac{u^*}{V}, \quad v = \frac{v^*}{V},$$ (54)

15

$$t = \frac{t^* V}{H}, \quad \rho = \frac{\rho^*}{\rho_0}, \quad p = \frac{p^*}{P}. \tag{55}$$

where the superscript * denotes the dimensional variables. The non-dimensional governing equations are obtained by defining the Reynolds number as $Re = \rho_0 V H / \eta$ and the Capillary number as $Ca = \eta V / \beta$:

$$\frac{d\rho}{dt} = -\rho \nabla \cdot \mathbf{u}, \tag{56}$$

$$\rho Re \frac{d\mathbf{u}}{dt} = \nabla \cdot \boldsymbol{\sigma} + \mathbf{F}_s + \mathbf{F}_v, \tag{57}$$

$$p(\rho) = Re c_0^2 (\rho - 1), \tag{58}$$

where

$$\mathbf{F}_v = \left(0, -\frac{1}{H^3} \right)^T \lambda, \tag{59}$$

$$\mathbf{F}_s = \frac{1}{Ca} \kappa \hat{\mathbf{n}} \lambda. \tag{60}$$

First, we consider the rupture of a liquid film with a moderate aspect ratio $\varepsilon = 0.5$. The computational domain is chosen as $-1 < x < 1$, $0 < y < 1$, so we have the width and height of liquid film $L = 2$ and $H = 1$, respectively. The initial particle spacing used is $\Delta x = 0.01$, with $L/\Delta x = 200$ layers of fluid particles along the x-direction and $H/\Delta x = 100$ along the y-direction. The Reynolds and capillary numbers are chosen to be $Re = 100$ and $Ca = 100$. To initiate the interfacial instability, a small downward velocity disturbance is imposed for all fluid particles at the start:

$$v = -0.1 \left[1 - \cos \left(2\pi \frac{x + L/2}{L} \right) \right]. \tag{61}$$

The sound speed is chosen as $c_0 = 200$. To maintain numerical stability, a time step of $\Delta t = 1 \times 10^{-5}$ is used. The particle shifting technique presented in [46] is adopted to maintain a homogeneous particle distribution. The solid substrate is modelled using wall and dummy particles [51], with the no-slip boundary condition on it. On the left and right sides of the liquid film, we impose periodic boundary conditions as in [1, 6, 54].

Fig. 8 shows the rupture process of the thin liquid film obtained by the present SPH model, where the magnitude of van der Waals force is indicated by the color bars. At the start, the small velocity disturbance reduces the film thickness at the midpoint of the domain ($x = 0$). As a result, the free surface particles there experience greater van der Waals forces, which in turn amplifies the downward velocity and the interface develops into a cusp. The lower the cusp is, the larger the magnitude of the van der Waals force becomes. This positive feedback leads to instability and the liquid film finally ruptures. Also, only one layer of fluid particles are used to model the van der Waals force, which shows that $\Lambda = 0.2$ in Eq. (33) is a good choice to identify the outmost layer free surface particles. There is no doubt that these particles delineate the interfacial profiles of liquid film. Of course, this value can slightly change with different kernel functions and different smoothing lengths. Moreover, the rupture point ($x=0$, $y=0$) is a singularity because the van der Waals force at this point goes to infinity according to Eq. (28). As a result, our simulation breaks down. This is, of course, a generic problem in simulating rupture and not a specific difficulty for SPH.
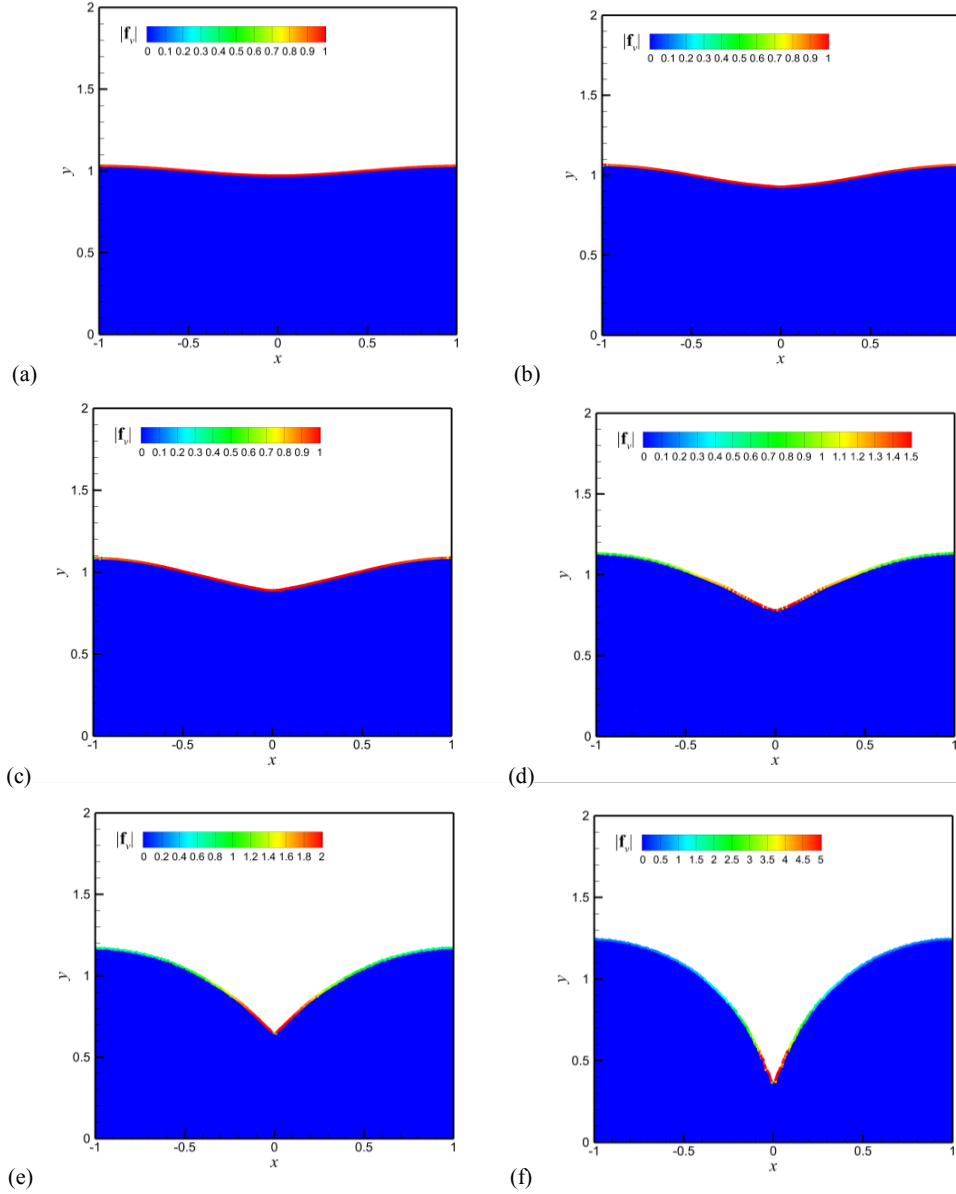
Fig. 8 SPH simulation of the rupture of a thin liquid film with $\varepsilon = 0.5$: the magnitude of van der Waals force $|\mathbf{f}_v|$ is displayed at dimensionless times $t = 2, 5, 7, 10, 12,$ and 14 from (a) to (f).

To better validate the present SPH method, it would be desirable to compare its predictions with those obtained by other numerical methods. Unfortunately, in the literature we have found no existing simulations of the liquid film breakup problem except those based on lubrication approximations [7–12]. Therefore, we will only demonstrate the convergence of the numerical solution by carrying out three additional runs with the initial particle spacing $\Delta x = 0.02$, 0.0125, and 0.0067. In these additional runs, all the other numerical parameters remain unchanged from those of Fig. 8. As seen in Fig. 9, three additional solutions and the original solution ($\Delta x = 0.01$) agree well at the early stage ($0 < t < 9$). In later stages, however, there is a delayed rupture as the particle resolution is decreased. Moreover, we also observe small upward jumps or jerks in the SPH trajectories, whose magnitude declines with finer resolution (see
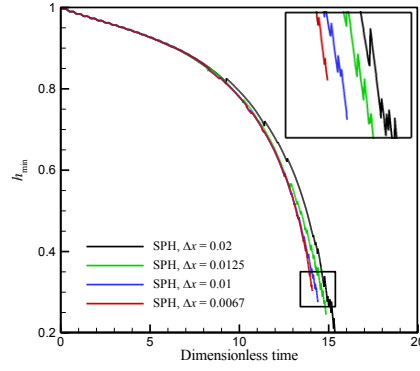
Fig. 9 The temporal evolution of the minimum film thickness h_{min}: the influence of particle spacing Δx on the SPH solutions.

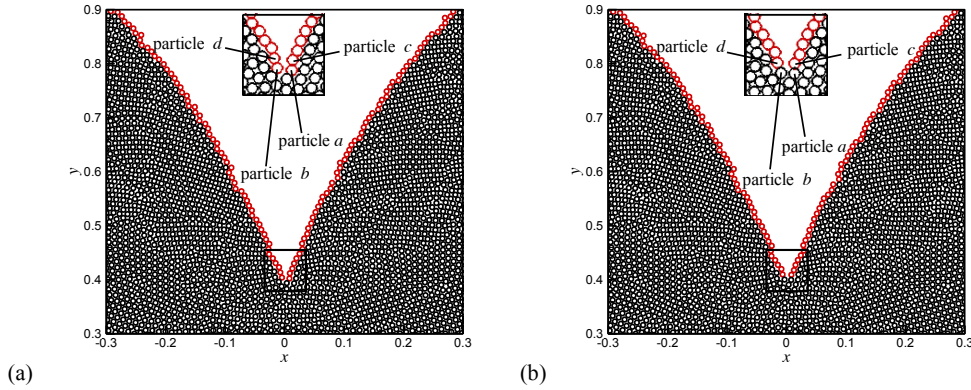(a)   (b)

Fig. 10 The jumping phenomenon in the minimum film thickness h_{min} at two consecutive time steps ($t = 13.7$ and 13.7001). The outmost layer of fluid particles are denoted by red circles while the inner particles are black circles.

magnified inset of Fig. 9). As our interface is represented by a layer of SPH particles, the cusp is identified with the particle with the smallest y-coordinate in this layer. This is how h_{min} is measured. However, as the cusp pushes downward, the interface is constantly extended. Thus, interior particles regularly come up to the interface in regions far from the cusp, while at the cusp, the surface particles are regularly drawn and absorbed into the bulk. This absorption is due to the tangential motion of particles along the interface towards the cusp. Each time the "cusp particle" joins the bulk, h_{min} is shifted onto the next lowest particle on the interface. This explains the recurrent upticks in the h_{min} curves.

Such an uptick is further illustrated in Fig. 10 by comparing the particle positioning at the cusp between two consecutive time steps. In Fig. 10a (at $t = 13.7$), the minimum film thickness h_{min} is recorded by the y-coordinate value of particle a. At the next time step (at $t = 13.7001$) in Fig. 10b, particles c and d have moved within each other's supporting domain. Their strong SPH interaction leads to them being identified as neighboring particles on the interface, while particles a and b are now considered interior particles. Consequently, particle c becomes the lowest surface particle that determines the minimum film thickness h_{min}. As the y-coordinate of particle c at the latter time step is larger than that of particle a at the
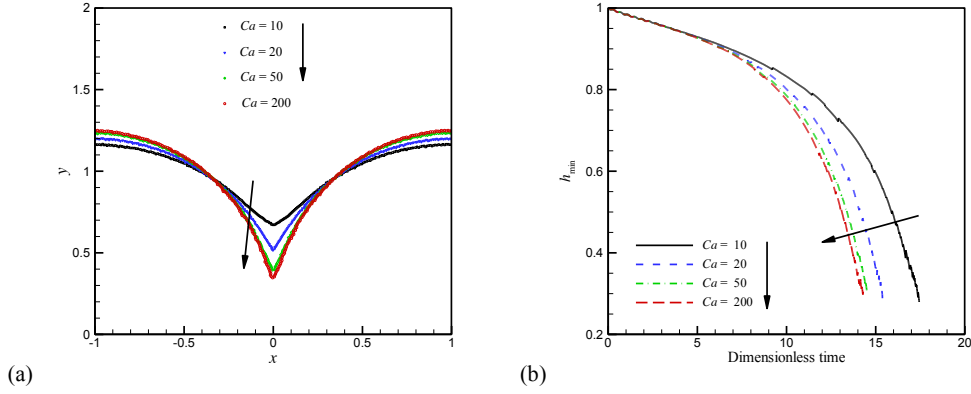
18

Fig. 11 The influence of capillary number on the rupture of thin liquid film: (a) the interfacial profiles at $t = 14$ and (b) the temporal evolution of the minimum film thickness h_{min}.

previous time step, a small uptick appears in the h_{min} curve. Therefore, the jumping phenomenon in Fig. 9 is a natural outcome of the particle representation of the interface, and the magnitude of the jumps decreases with refining particle spacing. If the SPH particles are sufficiently refined, the jumping phenomenon would become undetectable. However, in such a situation, the computational cost would be prohibitive. Even so, there are still only a few surface particles to model the van der Waals force and surface tension around the cusp. Therefore, the inadequate particle resolution at the sharp tip, which is ultimately inevitable as the tip becomes more pointed, is the root cause for the delayed rupture in SPH solutions. As a potential remedy, the adaptive particle refinement [58] may to a certain extent improve the accuracy of the spatial resolution of the sharp tip, but we will not explore this further in the present work.

To study the influence of the capillary number on the rupture process, four additional runs with $Ca = 10, 20\ 50,$ and 200 are performed, while all other parameters remain unchanged from Fig. 8. The smaller the capillary number is, the shallower the cusp at any given moment (Fig. 11a), and the slower the rupture process (Fig. 11b). A smaller capillary number corresponds to a larger surface tension coefficient. Since the surface tension resists interfacial deformation, its effect of stabilizing the film against rupture is easily understood.

We have also utilized the rupture of the liquid film with an aspect ratio $\varepsilon = 0.5$ (Fig. 8) to validate the coordinate transformation. Using $x = \tan(\xi)$, we transform the (x, y) domain to the new computational domain in (ξ, y): $-0.78 < \xi < 0.78, 0 < y < 1$. Then we solve the film rupture problem in the (ξ, y) domain with the same initial particle spacing $\Delta\xi = 0.01$ and the same parameters as in Fig. 8, using 15600 particles in the (ξ, y) domain as compared with 20000 particles in the (x, y) domain. The solution, transformed back to the (x, y) domain, is compared with that of Fig. 8 in Fig. 12. The two solutions agree very well in the interfacial profile. The minimum film thickness h_{min} agrees until $t = 13.5$. However, after that, the solution obtained in (ξ, y) slightly lags behind than that of (x, y). This is again a result of how SPH accounts for particle-particle interactions. Because of the shrinkage in the horizontal coordinate, the tip in (ξ, y) is always sharper than that in (x, y). In the later stage of rupture, the narrowing and deepening cusp in (ξ, y) induces stronger interaction across the tip and in turn the upward jump phenomenon noted in Fig. 9. This

19

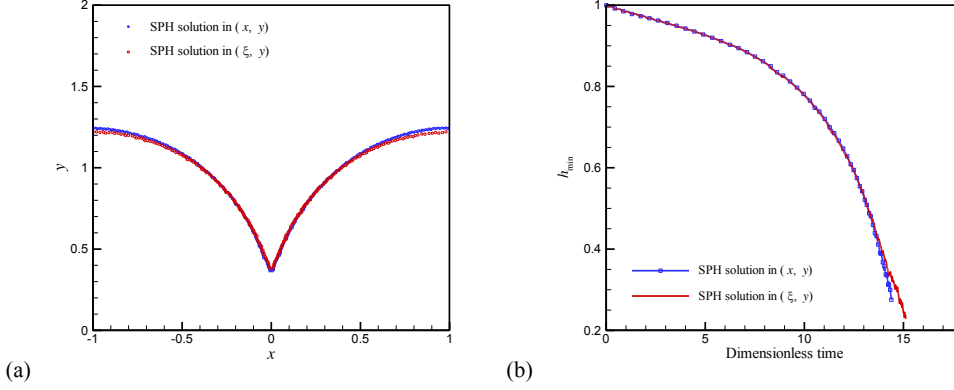explains the slight delay toward the end of rupture in the transformed domain.

(a)   (b)

Fig. 12 A comparison between SPH simulations in the (x, y) and (ξ, y) coordinates: (a) the interfacial profile at $t = 14$ and (b) the temporal evolution of the minimum film thickness h_{min}.

3.3.1 The case of a very small aspect ratio

Finally, we apply the proposed SPH method to simulate the rupture of a thin liquid film with a very small aspect ratio $\varepsilon = 0.005$. For this geometry, the computational domain is a long rectangle: $-100 < x < 100$, $0 < y < 1$. Resolving this long domain adequately using SPH particles would incur prohibitive computational costs. To avoid this problem, we apply the coordinate transformation along the x-axis, $x = \tan(\xi)$, as explained in Section 2.5.

The new computational domain is $-1.56 < \xi < 1.56$, $0 < y < 1$. The initial particle spacing in the (ξ, y) plane is still chosen as $\Delta\xi = 0.01$, which corresponds respectively to 312 and 100 layers of particles along the ξ- and y-direction, a saving of more than 64 times in the number of particles. All other numerical parameters are the same as those of Fig. 8. Fig. 13 depicts the evolution of the interfacial profile for the thin liquid film. The flow pattern of thin liquid film in the central region is similar to that of Fig. 8, where the liquid film finally ruptures. However, there are two visible differences from Fig. 8. First, there is a hump on each side of the cusp, with the liquid rising up. Besides, the liquid level at the two ends of the domain ($\xi = 1.56$ and -1.56) hardly changes. In Fig. 8, there is no hump and the liquid level rises appreciably on the ends of the domain. Both differences are consequences of the very great length of the film in the physical (x, y) domain. The lowering of the interface near the cusp has to be accompanied by a rise of the liquid level to maintain mass conservation. However, given the very large x-dimension in Fig. 13, the rise has yet to propagate to the ends. This is, in essence, the same phenomenon as the rising liquid level of Fig. 8, where the ends of the domain ($x = 1$ and -1) is at comparable distances from the cusp as the humps are in Fig. 13. We note that the humped profile has been reported in solutions under lubrication approximations [55], whose qualitative feature is similar to our SPH solution with coordinate transformation.

As a more quantitative verification, we compare with the solution of Burrelbach et al. [56] who used the lubrication approximation to study the breakup of a liquid film similar to the one considered in the

current study. Note that Burrelbach et. al. [56] used a domain of length $\lambda_m\ (=2\pi/k_m)$, where $k_m = 1/\sqrt{2}$ is the wavenumber corresponding to the dominant mode of linear instability calculated by William and Davis [8].
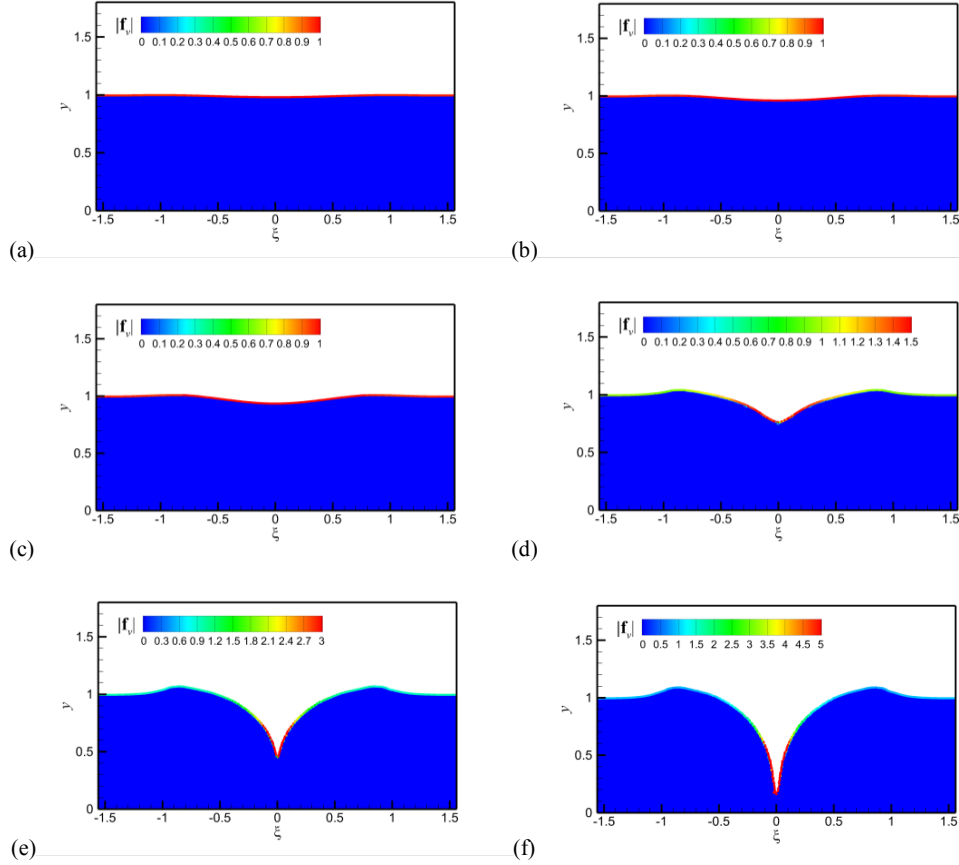

Fig. 13 SPH simulations of the rupture of a thin liquid film with $\varepsilon = 0.005$: the magnitude of van der Waals force $\mathbf{f}_v$ is displayed at $t = 2, 5, 7, 11, 13,$ and 15.4 from (a) to (f).

Fig. 14 compares the interfacial profiles of both studies just before rupture, with our computational domain truncated to the central portion of the same length. The surface profiles agree reasonably well close to the breakup. Burrelbach et. al. [56] also reported a breakup time of $t_B \approx 4.93$ (after conversion to our dimensionless time) while our calculation predicts a much longer time of 15.4. This difference can be attributed to the different numerical setups of two studies. In [56], the simulation started from an interfacial height disturbance: $h(x,t)=1+0.1\sin(k_m x)$. On the other hand, our SPH calculations start from an initial velocity disturbance given by Eq. (61). Otherwise, SPH would require an excessively large number of uniformly distributed particles at the start of the simulation to resolve the slight interfacial deformation. With our initial interfacial velocity, it takes a finite time ($0 < t < 8.7$) for the flat interface to deform into the sinusoidal shape of the same amplitude as the initial condition of [56]. Considering this difference, our adjusted breakup time is $t_B \approx 6.7$, which is comparable to Burrelbach et. al.'s result. We also highlight that our longer breakup time is again the consequence of the recurrent upticks as explained in the case of $\varepsilon = 0.5$. Since the classical lubrication theory does not easily admit an initial velocity perturbation, we have not

striven for a more direct quantitative comparison on the breakup time in the current study.
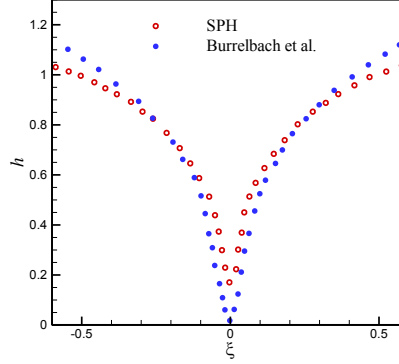

Fig. 14 A comparison of the interfacial profiles just before rupture, at $t = 4.96$ in Burrelbach et. al. [56] and $t = 15.4$ in the current SPH simulation.

4. Conclusions

In this paper, we have developed an SPH representation for the van der Waals force and simulated the rupture of thin liquid films without resort to lubrication theory. The van der Waals force is modelled by a surface force imposed on the surface layer of particles only, and the surface tension is modelled in a similar way. In either case, we have defined a surface weighting function to properly identify the surface layer of particles, which effectively eliminates the ambiguity that may arise when resolving highly deformed surfaces using particles. To allow the extreme aspect ratio of very thin and long liquid films, we have also introduced a coordinate transformation to shrink the longitudinal coordinate far from the central area of rupture. The algorithms are tested by simulating a series of problems and comparing, to the extent possible, with known solutions in the literature. The following conclusions can be drawn from the results.

(1) Our SPH scheme of modelling the van der Waals force is reasonable and reliable, and it produces the correct hydrostatic pressure field in the interior of the film.

(2) By simulating the relaxation of an initially square droplet as verification, we have established the accuracy and stability of the surface tension model.

(3) The coordinate transformation can efficiently deal with the rupture of a thin liquid film with a very small aspect ratio, producing accurate results at reduced cost.

(4) The rupture of thin liquid films is accompanied by two humps on either side of the cusp, which propagates outward from the point of rupture.

Compared with mesh-based methods, SPH has a unique advantage in its ability of representing the process of rupture and coalescence directly. The innovations of this work, including the models for van der Waals force and interfacial tension as well as the coordinate transformation, have opened up the problem of thin film dynamics to SPH simulations. In the near future, we anticipate applications of the SPH algorithm

to an array of interesting problems, ranging from tear-film breakup [6] to dryout in heat exchangers [57].In terms of algorithms, the current model can be extended by an adaptive particle refinement algorithm [58], which may further improve the accuracy of the spatial resolution of the interfacial cusp toward the end of the rupture of the thin liquid film.

Acknowledgements

References

[1] A. Oron, S.H. Davis, S.G. Bankoff, Long-scale evolution of thin liquid films, Rev. Mod. Phys. 69(1997) 931-980.

[2] S.J. Weinstein, K.J. Ruschak, Coating flows, Annu. Rev. Fluid Mech. 36(2004) 29-53.

[3] P. Yu, W. Zhou, S. Yu, Laser-induced local heating and lubricant depletion in heat assisted magnetic recording systems, Int. J. Heat Mass Transfer 59(2013) 36-45.

[4] S. Cohen-Addad, R. Höhler, O. Pitois, Flow in foams and flowing foams, Annu. Rev. Fluid Mech. 45(2013) 241-267.

[5] R.J. Braun, Dynamics of the tear film, Annu. Rev. Fluid Mech. 44(2012) 267-297.

[6] M. Dey, A.S. Vivek, H.N. Dixit, A. Richhariya, J.J. Feng, A model of tear-film breakup with continuous mucin concentration and viscosity profiles, J. Fluid Mech. 858(2019), 352-376.

[7] E. Ruckenstein, R.K. Jain, Spontaneous rupture of thin liquid films, J. Chem. Soc., Faraday Trans. 2, 70(1974) 132-147.

[8] M.B. Williams, S. H. Davis, Nonlinear theory of film rupture, J. Colloid Interface Sci. 90(1982) 220-228.

[9] W.W. Zhang, J.R. Lister, Similarity solutions for van der Waals rupture of a thin film on a solid substrate, Phys. Fluids 11(1999) 2454-2462.

[10] D.T. Conroy, R.V. Craster, O.K. Matar, et al. Dynamics and stability of an annular electrolyte film, J. Fluid Mech. 656(2010) 481-506.

[11] V. Garg, P.M. Kamat, C.R. Anthony, et al. Self-similar rupture of thin films of power-law fluids on a substrate, J. Fluid Mech. 826(2017) 455-483.

[12] C.W. Hirt, B.D. Nicholls, Volume of fluid (VOF) method for dynamics of free boundaries, J. Comput. Phys. 39 (1981) 201–221.

[13] S. McKee, M.F. Tomé, V.G. Ferreira, et al. The MAC method, Comput. Fluids. 37 (2008) 907–930.

[14] S. Osher, J.A. Sethian, Fronts propagating with curvature-dependent speed: algorithms based on Hamilton Jacobi formulations, J. Comput. Phys. 79 (1988) 12–49.

[15] G.R. Liu, M.B. Liu, Smoothed Particle Hydrodynamics: A Meshfree Particle Method, World Scientific, Singapore, 2003.

[16] L.B. Lucy, A numerical approach to the testing of the fission hypothesis, Astron. J. 83 (1977) 1013–1024.

[17] R.A. Gingold, J.J. Monaghan, Smoothed particle hydrodynamics theory and application to non-spherical stars, Mon. Not.

R. Astron. Soc. 181 (1977) 375–389.

[18] S.M. Hosseini, J.J. Feng, A particle-based model for the transport of erythrocytes in capillaries, Chem. Eng. Sci. 64(2009) 4488-4497.

[19] H. Gotoh, A. Khayyer, On the state-of-the-art of particle methods for coastal and ocean engineering, Coast. Eng. J. 60(2018) 79-103.

[20] M.B. Liu, G.R. Liu, Z. Zong, K.Y. Lam, Computer simulation of high explosive explosion using smoothed particle hydrodynamics methodology, Comput. Fluids. 32(2003):305–322

[21] M.B. Liu, Z.L. Zhang, D.L. Feng, A density-adaptive SPH method with kernel gradient correction for modeling explosive welding, Comput. Mech. 60 (2017) 513–529.

[22] A. Zhang, P. Sun, F. Ming, et al. Smoothed particle hydrodynamics and its applications in fluid-structure interactions, J. Hydrodynamics 29(2017) 187-216.

[23] Z. B. Wang, R. Chen, H. Wang, Q. Liao, X. Zhu, S. Z. Li, An overview of smoothed particle hydrodynamics for simulating multiphase flow, Appl. Math. Model. 40 (2016) 9625–9655.

[24] X. Xu, J. Ouyang, T. Jiang, Q. Li, Numerical simulation of 3D-unsteady viscoelastic free surface flows by improved smoothed particle hydrodynamics method, J. Non-Newtonian. Fluid Mech. 177 (2012) 109–120.

[25] X. Xu, J. Ouyang, A SPH-based particle method for simulating 3D transient free surface flows of branched polymer melts, J. Non-Newtonian. Fluid Mech. 202 (2013) 54–71.

[26] X. Xu, J. Ouyang, Q. Liu, W. Li, SPH simulations of 2D transient viscoelastic flows using Brownian configuration fields, J Non-Newtonian Fluid Mech 208 (2014) 59–71.

[27] X. Xu, P. Yu, A multiscale SPH method for simulating transient viscoelastic flows using bead-spring chain model, J Non-Newtonian Fluid Mech 229 (2016) 27–42.

[28] S. Nugent, H.A. Posch, Liquid drops and surface tension with smoothed particle applied mechanics, Phys. Rev. E 62 (2000) 4968.

[29] A.M. Tartakovsky, P. Meakin, Modeling of surface tension and contact angles with smoothed particle hydrodynamics, Phys. Rev. E 72(2005) 1–9.

[30] J.U. Brackbill, D.B. Kothe, C. Zemach, A continuum method for modeling surface tension, J. Comput. Phys. 100 (1992) 335–354.

[31] J.P. Morris, Simulating surface tension with smoothed particle hydrodynamics, Int. J. Numer. Methods Fluids 33(2000) 333–353.

[32] X.Y. Hu, N.A. Adams, A multi-phase SPH method for macroscopic and mesoscopic flows, J. Comput. Phys. 213 (2006) 844–861.

[33] N. Grenier, M. Antuono, A. Colagrossi, D. Le Touzé, B. Alessandrini, An Hamiltonian interface SPH formulation for multi-fluid and free surface flows, J. Comput. Phys. 228 (2009) 8380–8393.

[34] A. Zainali, N. Tofighi, M. Shadloo, M. Yildiz, Numerical investigation of Newtonian and non-Newtonian multiphase flows using ISPH method, Comput. Methods Appl. Mech. Engrg. 254(2013) 99–113

[35] M. Zhang, X.L. Deng, A sharp interface method for SPH, J. Comput. Phys. 302 (2015) 469–484.

[36] A. Krimi, M. Rezoug, S. Khelladi, et al. Smoothed particle hydrodynamics: A consistent model for interfacial multiphase fluid flow simulations, J. Comput. Phys. 358(2018) 53-87.

[37] J.J. Monaghan, Simulating free surface flows with SPH, J. Comput. Phys.110 (1994) 399–406.

[38] M.B. Liu, G.R. Liu, Smoothed particle hydrodynamics (SPH): an overview and recent developments, Arch. Comput. Methods Eng. 17 (2010) 25–76.

[39] H. Wendland , Piecewise polynomial, positive definite and compactly supported radial functions of minimal degree, Adv. Comput. Math. 4 (1995) 389–396 .

[40] J. Bonet, T.-S.L. Lok, Variational and momentum preservation aspects of smooth particle hydrodynamic formulations,

Comput. Methods Appl. Mech. Engrg. 180 (1999) 97–115.

[41] M.B. Liu, G.R. Liu, Restoring particle consistency in smoothed particle hydrodynamics, Appl. Num. Math. 56 (2006) 19–36.

[42] R.C. Batra, G.M. Zhang, SSPH basis functions for meshless methods, and comparison of solutions with strong and weak formulations, Comput. Mech. 41 (2008) 527–545.

[43] G.M. Zhang, R.C. Batra, Symmetric smoothed particle hydrodynamics (SSPH) method and its application to elastic problems, Comput. Mech. 43 (2009) 321–340.

[44] A. Ferrari, M. Dumbser, E.F. Toro, A. Armanini, A new 3D parallel SPH scheme for free-surface flows, Comput. Fluids 38 (2009) 1203–1217.

[45] X. Xu, X. L. Deng, An improved weakly compressible SPH method for simulating free surface flows of viscous and viscoelastic fluids, Comput. Phys. Commun. 201(2016) 43–62.

[46] X. Xu, P. Yu, A technique to remove the tensile instability in weakly compressible SPH, Comput. Mech. 62(2018) 963–990.

[47] S. Adami, X.Y. Hu, N.A. Adams, A new surface-tension formulation for multi-phase SPH using a reproducing divergence approximation, J. Comput. Phys. 229 (2010) 5011–5021.

[48] B.M. Stupovski, J. V. Crnjanski, D.M. Gvozdić, Application of coordinate transformation and finite differences method in numerical modeling of quantum dash band structure, Comput. Phys. Commun. 182(2011) 289-298.

[49] O. Ozgun, M. Kuzuoglu, Implementation of coordinate transformations in periodic finite element method for modeling rough surface scattering problems, Int. J. RF Microwave Computer Aided Eng. 26(2016) 322-329.

[50] S. Adami, X.Y. Hu, N.A. Adams, A generalized wall boundary condition for smoothed particle hydrodynamics, J. Comput. Phys. 231(2012) 7057–7075.

[51] X. Xu, An improved SPH approach for simulating 3D dam-break flows with breaking waves, Comput. Methods Appl. Mech. Engrg. 311(2016) 723-742.

[52] X. Xu, P. Yu, Extension of SPH to simulate non-isothermal free surface flows during the injection molding process, Appl. Math. Model. 73 (2019) 715–731.

[53] A. Colagrossi, M. Landrini, Numerical simulation of interfacial flows by smoothed particle hydrodynamics, J. Comput. Phys. 191 (2003) 448–475.

[54] Y. L. Zhang, O.K. Matar, R.V. Craster, Analysis of tear film rupture: effect of non-Newtonian rheology, J. Colloid Interface Sci. 262(2003) 130-148.

[55]Y. L. Zhang, R.V. Craster, O.K. Matar, Surfactant driven flows overlying a hydrophobic epithelium: film rupture in the presence of slip, J. Colloid Interface Sci. 264(2003) 160-175.

[56] J. P. Burelbach, S.G. Bankoff, S.H. Davis, Nonlinear stability of evaporating/condensing liquid films, J. Fluid Mech. 195(1988) 463-494.

[57] H. Li, H. Anglart, Prediction of dryout and post-dryout heat transfer using a two-phase CFD model, Int. J. Heat Mass Transfer 99(2016) 839-850.

[58] L. Chiron, G. Oger, M. De Leffe, D. Le Touzé, Analysis and improvements of Adaptive Particle Refinement (APR) through CPU time, accuracy and robustness considerations, J. Comput. Phys. 354 (2018) 552–575.